Nanoscale

PAPER

Check for updates

Order–disorder transition in nano-rutile TiO$_2$ anodes: a high capacity low-volume change Li-ion battery material†

Christian Kolle Christensen,[a] Mohammad Aref Hasen Mamakhel,[b] Ananya Renuka Balakrishna,[c] Bo Brummerstedt Iversen, [b] [b] Yet-Ming Chiang [c] [c] and Dorthe Bomholdt Ravnsbæk [b] *[a]

Nano-sized particles of rutile TiO$_2$ is a promising material for cheap high-capacity anodes for Li-ion batteries. It is well-known that rutile undergoes an irreversible order–disorder transition upon deep discharge. However, in the disordered state, the Li$_x$TiO$_2$ material retains a high reversible ion-storage capacity of >200 mA h g^{-1}. Despite the promising properties of the material, the structural transition and evolution during the repeated battery operation has so far been studied only by diffraction-based methods, which only provide insight into the part that retains some long-range order. Here, we utilize a combination of *ex situ* and *operando* total scattering with pair distribution function analysis and transmission electron microscopy to investigate the atomic-scale structures of the disordered Li$_x$TiO$_2$ forming upon the discharge of nano-rutile TiO$_2$ as well as to elucidate the phase behavior in the material during the repeated charge–discharge process. Our investigation reveals that nano-rutile upon Li-intercalation transforms into a composite of ~5 nm domains of a layered Li$_x$TiO$_2$ α-NaFeO$_2$-type structure with ~1 nm Li$_x$TiO$_2$ grain boundaries with a columbite-like structural motif. During repeated charge–discharge cycling, the structure of this composite is retained and stores Li through a complete solid–solution transition with a remarkably small volume change of only 1 vol%.

Introduction

Titanium dioxide is a highly versatile material known to function as a photocatalyst,[1,2] photovoltaic,[3] and supercapacitor[4] and for photo-electrochemical water splitting.[4,5] Recently, TiO$_2$ has proven to be a promising alternative to commercial Li$_4$Ti$_5$O$_{12}$ and carbon-based anodes for Li-ion batteries,[6–10] due to its low production cost, high capacity and low environmental impact.[11] The theoretical capacity of TiO$_2$

[a] *Department of Physics, Chemistry and Pharmacy, University of Southern Denmark, Campusvej 55, 5230 Odense M, Denmark. E-mail: dbra@sdu.dk*
[b] *Center for Materials Crystallography, Department of Chemistry and iNANO, Aarhus University, Langelandsgade 140, 8000 Aarhus C, Denmark*
[c] *Department of Materials Science and Engineering, Massachusetts Institute of Technology, 77 Massachusetts Ave., Cambridge, MA 02139, USA*

†Electronic supplementary information (ESI) available: Overview of known ambient-condition TiO$_2$ polymorphs; PDF analysis of as-prepared rutile TiO$_2$ nanoparticles; GITT data, Le bail fits of PXRD data for the chemically lithiated LiTiO$_2$ material; Raman spectra of chemically lithiated Li$_x$TiO$_2$ samples; PDF analysis exploring different TiO$_2$ polymorphs as local phases; illustration of the close packed stacking sequence of O3-type and O2-type AMO$_2$ structures; PDF analysis of the chemically lithiated sample using O3-type, O2-type and the distorted α-NaFeO$_2$-type; the result of fracture mechanics analysis. See DOI: 10.1039/c9nr01228a
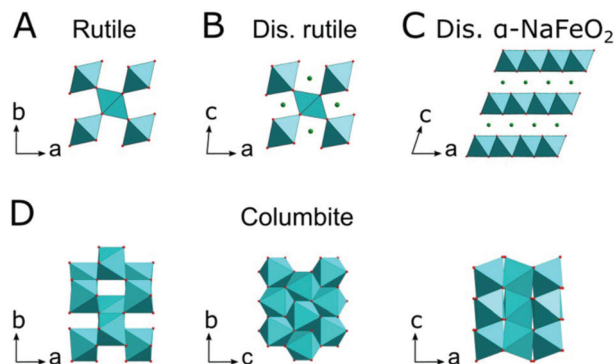
(335 mA h g^{-1}) is excellent in comparison with Li$_4$Ti$_5$O$_{12}$ (175 mA h g^{-1}) and decent compared to graphite (372 mA h g^{-1}). The discharge potential is significantly higher, typically 1.5 to 1.8 V *vs.* Li compared to <0.5 V for graphite. This results in the lower energy density of the cells; however, higher anode potential reduces the risks of Li-plating and electrolyte decomposition at the anode, which enhances cycle life and battery safety, especially when operating at high rates.

Under ambient conditions, eight TiO$_2$ polymorphs are currently known: anatase, rutile, brookite, TiO$_2$-B (bronze), TiO$_2$-H (hollandite), TiO$_2$-R (ramsdellite), TiO$_2$-II (columbite) and TiO$_2$-III (baddeleyite) (see further details in Table S1, ESI†). The former four have been widely explored as anode materials in Li-ion batteries. Rutile is a natural choice as it is the thermodynamic stable polymorph and its structure contains one-dimensional channels along the *c*-axis (Fig. 1A), allowing for Li-insertion and -extraction. Unfortunately, in the bulk form, rutile exhibits limited storage capacities of <0.1Li per TiO$_2$ at room temperature,[12,13] and temperatures of ≥120 °C are required to achieve reversible Li-ion storage.[14–16] The poor Li-intercalation in bulk rutile has been associated with the blocking of the channels parallel to the *c*-axis along which the diffusion coefficient is nine orders of magnitude higher than that in the *ab*-plane.[17–19] Fortunately, the Li-ion storage

Fig. 1 Crystal structures of TiO_2 and Li_xTiO_2 polymorphs relevant in this study: (A) rutile, (B) monoclinic distorted rutile, Li_xTiO_2 ($P2/m_{RUT}$), (C) monoclinic distorted α-NaFeO$_2$-type Li_xTiO_2 ($P2/m_{HEX}$) and (D) columbite, TiO_2–II, viewed along the three unit cell axis. The [TiO_6] octahedra are shown as light blue polyhedra and Li as green spheres.

capacity can be significantly improved by utilizing nano-sized rutile particles.[10,20–23] Previous studies suggest that the smaller the particles, the higher the Li-ion storage capacity,[24] e.g. spherical particles of 50 nm diameter intercalates 0.23Li per TiO_2, while nanorods with a cross-section of 10 nm intercalate 0.85Li,[23] which corresponds to a capacity of 285 mA h g^{-1}.

During Li-insertion in nano-sized rutile, several phase transitions have been reported and it appears that there is some variation in the structural evolution depending on particle size and morphology. A monoclinic distorted lithiated rutile, Li_xTiO_2 has been observed with an intercalation of up to ~0.5Li per TiO_2 (Fig. 1B).[25–27] This phase has been observed in both theoretical and experimental studies.

The structure has been described using various space group symmetries, but, based on neutron diffraction, the space group $P2/m$ (often denoted as $P2/m_{RUT}$) seems to be a good choice.[25] With Li-insertion beyond ~0.5Li, a two-phase transition is observed. The appearing phase has a low degree of crystallinity and only a few broad Bragg reflections are generally observed.[21,23,25,28,29] This complicates the analysis using traditional diffraction methods, which so far have been the main tool in the structural investigations. Diffraction data have however allowed for indexing and several structures have been suggested, i.e. an $Fm\bar{3}m$ rock salt structure, an $R\bar{3}m$ hexagonal[30] structure and a closely related $P2/m$ monoclinic structure. In the rock salt structure, the cations may be randomly distributed on the octahedral sites in the cubic close packed (ccp) oxygen lattice, while in the latter two structures, the cations are ordered within the ccp oxygen lattice such that alternating Ti- and Li-layers are formed (Fig. 1C). The hexagonal structure is an α-NaFeO$_2$-type structure, which also represents other very well-known electrode materials of the $LiMO_2$ family, e.g. $LiCoO_2$ and $Li(Ni,Mn,Co)O_2$ (the so-called NMC).[30] The $P2/m$ structure is simply a monoclinic distortion of the hexagonal structure and is thus often denoted as $P2/m_{HEX}$ not to confuse it with $P2/m_{RUT}$. The $P2/m_{HEX}$ structural model has

been confirmed by both powder neutron diffraction and first-principles calculations.[25,26]

Hence, previous investigations provide some insight into the evolution of the long-range order structures in nano-rutile during Li-insertion with the assignment of various crystalline phases. However, detailed knowledge is lacking on several levels. Firstly, and most importantly, the transformations beyond an insertion of ~0.5Li per TiO_2 results in a significant loss of crystallinity, which simply cannot be explained by crystalline-to-crystalline phase transformation, but must involve amorphization, cracking or nano-crystallization. Secondly, the structural transformations and the underlying mechanism of repeated Li-extraction and -insertion in the disordered Li_xTiO_2 phase remains unexplored. Thirdly, the relationship between the observed Li_xTiO_2 polymorphs and the cause of the structural transformations have not been discussed in detail. These questions prompted us to investigate the phase transformation pathway of nano-rutile anodes. To probe both the crystalline and disordered phases in the anode, we utilize a combination of powder X-ray diffraction (PXRD), total X-ray scattering (TXS) with pair distribution function (PDF) analysis and transmission electron microscopy (TEM). To achieve insight into the true dynamic transformation pathways, the X-ray scattering experiments were conducted under *operando* conditions. Several recent studies have shown that the structural evolution during the battery charge–discharge process may differ significantly between static (*ex situ*) and dynamic (*operando*) conditions,[31–34] as battery operating conditions inherently are far from equilibrium. Through the combination of these techniques and data refinement, a complete overview of the phase transformations is obtained, and the nature of the disorder induced during discharge is explained. Furthermore, the study reveals the structural phase transformation mechanism during repeated cycling of nano-rutile anodes.

Experimental

Synthesis of TiO_2 rutile nanoparticles

The synthesis of the TiO_2 rutile nanoparticles are described in a paper by Mamakhel *et al.*[35] Herein, 200 mL of 1.6 M HCl solution was kept under magnetic stirring and a mixture of 25 mL titanium(IV) isopropoxide, $Ti(OC_3H_7)_4$ (97%, Sigma-Aldrich), and 25 mL isopropanol (99.8%, Sigma-Aldrich) was added. Initially, a white suspension was obtained, which after heating dissolved to give a clear solution. The transparent solution was heated in a Teflon-lined autoclave at 200 °C for 12 h and subsequently cooled to room temperature. The resulting titanium dioxide powders were separated in a centrifuge (7000 rpm for 10 min), washed several times with deionized water and ethanol and dried at 105 °C overnight in a vacuum oven.

Electrochemical cell assembly and electrochemical characterization

The as-prepared TiO_2 nanoparticles were mixed in acetone with carbon (SuperP C45) and poly(vinylidene fluoride) (PVDF)

in a weight ratio of 8 : 1 : 1 wt%. The slurry was coated onto a glass plate, left to dry and scraped off to obtain a powdered mixture. The mixture was uniaxially pressed into Ø 6 mm free standing pellets of approx. 12 mg. Galvanostatic cycling and galvanostatic intermittent titration (GITT) tests were performed in two electrode Swagelok cells with Li foil as the counterelectrode and Whatman GF/B separator soaked with seven drops of 1 M LiPF$_6$ in ethylene carbonate : dimethyl carbonate 1 : 1 v/v (99.9%, Solvionic). Galvanostatic cycling was performed in a potential window of 1.0 to 3.0 V with a current density of 33.5 mA h g^{-1} (C/10) unless otherwise noted.

Chemical lithiation

The TiO$_2$ nanoparticle powders were dried for 2 days under vacuum at 60 °C. Approximately 25 mg of the particles were suspended in anhydrous heptane, and 0.5, 0.8, and 1.0 mole equivalents of n-butyllithium (1.6 M in hexane) were added to the suspensions under magnetic stirring in an argon atmosphere. The mixtures were left to react for two days and the remaining liquid was removed. The powders were washed in heptane and twice with acetone and dried to obtain powders ranging from a slightly pale blue color to dark blue, almost black.

X-ray diffraction and total scattering

Powdered samples for ex situ powder X-ray diffraction (PXRD) and total X-ray scattering (TXS) were mounted in polyimide tubes (1.0 mm inner diameter, Cole-Parmer). The ex situ PXRD and TXS data of pristine and chemically lithiated samples were collected at beamline ID-11-B at APS, Argonne, USA with a wavelength of 0.2113 Å. For operando SR-PXRD and TXS, the cathode pellets were mounted in AMPIX-type battery cells[36] specially designed for X-ray scattering experiments. The cathode pellets were mounted together with 14 mm discs of Whatman GL/B separators wetted by LiPF$_6$ electrolyte as mentioned above and 12 mm diameter discs of the Li-metal anode. The operando PXRD and TXS were performed at the P02.1 beamline at PETRAIII at DESY, Hamburg, Germany with an X-ray wavelength of 0.2073 Å. Scattering patterns were collected using total exposure times of 30 and 240 s per PXRD and TXS pattern, respectively. A pattern was collected every ~6 min for PXRD and ~30 min for TXS. Scattering patterns (at both PETRAIII and APS) were collected using a PerkinElmer (XRD1621) area detector. A CeO$_2$ standard placed at the cathode pellet position in the AMPIX cell was used for calibration. Diffraction spots originating from the anode metal were masked before azimuthal integration of the raw scattering data using the Fit2D software.[37] All patterns (for PXRD and TXS, separately) were scaled to compensate for beam intensity fluctuations using the intensity of the primary beam shoulder average over a 2θ or q-range at small angles. Sequential Rietveld refinements were performed using the FullProf software, a fitting scale factor, the cell parameters and FWHM parameter W. For the Scherrer crystallite size analysis, the data for the CeO$_2$ standard were used to correct for instrumental broadening. The TXS data were treated using the PDFgetX3

software[38] with an upper Q-range cutoff ($Q_{\text{max-inst}}$) at 21 Å^{-1} and 24 Å^{-1} for operando and ex situ, respectively, and the r_{poly} value was set to 0.9 Å to obtain PDFs. The structural models were fitted in real space to the PDF data using the PDFgui software.[39] For fitting the operando data, a graphite phase was included to account for the uncompleted subtraction of the background carbon signal from the AMPIX cell windows and conductive carbon in the pellet (see Fig. S1, ESI†). The result from the fitting ex situ data of the pristine material was used with fixed parameters to fit a graphite phase to the remaining carbon signal in the first scan of the operando data. This procedure is preferred instead of simply subtracting a scaled graphite PDF signal, as it allows for small adjustments of the scale and in-plane cell parameter, a, of the graphite component and thereby also for monitoring that the residual signal remains constant in the sequential fitting.

Electron microscopy

Transmission electron microscopy (TEM) was performed using a JEOL 2010FEG microscope operated with an acceleration voltage of 200 kV.

Raman spectroscopy

Raman spectra were recorded on a Renishaw inVia Reflex Micro Raman spectrometer using a 532 nm 75 mW laser operated at 10% power. The spectra of the powders were recorded with an exposure time of 1 s using a 10× objective.

Fracture analysis

Following Hu et al.,[40] we assume pre-existing crack-like flaws in the rutile electrode particle. During a typical charge/discharge cycle, the particle is stressed by lattice mismatch between the lithiated and delithiated phases. This stressed interface contributes to elastic energy in the particle, which can be reduced by electrode fracture.[41,42] However, the fracture is accompanied by the formation of two interfaces that increase the surface energy of the system. Therefore, the electrode fracture is suppressed when the energy release rate from crack propagation G is less than the surface energy 2γ. The energy released from crack propagation G is a function of electrode geometry Z, elastic modulus E, mismatch strain ε and electrode particle size d. The electrode fracture is suppressed for:

$$G(Z, E, \varepsilon, d) < 2\gamma$$

$$d_{\text{crit}} = \frac{2\gamma}{ZE\varepsilon^2}.$$

To determine the critical particle size d_{crit} for rutile electrodes, we model an equiaxed particle of size 4 μm × 4 μm × 2 μm in ABAQUS. The elastic constants of rutile used in the finite element simulations were obtained from Murphy et al.[43] The electrode particle deforms during lithium insertion, and the corresponding anisotropic axial strains used in the calculations were $\varepsilon_{11} = 4.76\%$ $\varepsilon_{22} = 2.92\%$ and $\varepsilon_{33} = 1.08\%$. Further details of the finite element procedure can be found in ref. 39.

Overall, the calculation estimates the critical particle size for rutile electrodes below which crack propagation is suppressed to be $d \sim 20$ nm.

Results and discussion

The phase pure rutile TiO_2 nanoparticles were prepared by hydrothermal synthesis as described by Mamakhel *et al.*[35] The as-prepared nanoparticles are elongated with a diameter of d = 7–15 nm and a length of L = 15–50 nm, which is confirmed by TEM. Analysis of the PDF obtained from the TXS data reveals that the structure of the as-prepared rutile is better described using a small monoclinic distortion in the space group symmetry $P2/m_{RUT}$ (R_w = 12%) compared to the traditional tetrahedral $P4_2/mnm$ symmetry (R_w = 14%) of rutile (see Fig. S2 and Table S2, ESI†). The monoclinic distortion causes only a slight distortion of the $[TiO_6]$ octahedra as seen from the comparison in Fig. 1. Fitting the spherical diameter of the particles in the PDF analysis provides an estimated size of 10–11 nm.

In the first discharge, the nano-rutile anode takes up ~1Li before reaching the lower potential limit of 1.0 V (Fig. 2). In accordance with previous reports, the galvanostatic potential profile can be divided into three regimes: sloping potential up to an insertion of ~0.15Li per TiO_2 followed by two plateau-like regions at ~1.4 and ~1.15 V, respectively (see also the galvanostatic intermittent titration data in Fig. S3, ESI†). From *operando* PXRD (Fig. 2A), it is evident that an insertion of the initial ~0.7Li occurs *via* a solid solution reaction as the Bragg reflections from the rutile structure change the angular position continuously and no new peaks appear. The rutile Li_xTiO_2 phase is nicely simulated by the Rietveld refinement of the *operando* PXRD data up to an insertion of xLi = 0.78, provided that the monoclinic distorted rutile-like structure ($P2/m_{RUT}$) is used as the structural model in the refinement. The continuous change in lattice parameters during the first Li-insertion is not as pronounced in the PDF overview (Fig. 2B) as in the PXRD data, since a small change in lattice parameters is not amplified in the PDFs as in the diffraction case, where $2\theta = 2\sin^{-1}(\lambda/d)$. However, fitting the PDF data using the same $P2/m_{RUT}$ structural model provides a good fit and nearly identical unit cell parameters. After an insertion of 0.78Li, the Rietveld refinement of the PXRD data fails as the Bragg peaks of the monoclinic $P2/m_{RUT}$ Li_xTiO_2 become too diffuse. Concurrently, two new peaks appear in the diffraction data at $2\theta \sim 5.5$ and 8° (possibly also at 4° and 5°). Hence, the evolution of the Bragg reflections at the end of the first discharge clearly suggests a two-phase transition between $P2/m_{RUT}$ Li_xTiO_2 and a new disordered or nanocrystalline Li-rich phase with significantly broadened Bragg peaks in comparison with the peaks from the original rutile structure. The crystallite size of the new phase determined by the Scherrer equation (assuming no strain contribution) is ~4.5(5) nm at the end of discharge. The Bragg peaks from the appearing Li-rich phase can be indexed in a cubic $Fm\bar{3}m$ cell (a = 4.1282(4) Å) or two different monoclinic $P2/m$ cells (a = 5.0144(19) Å, b = 2.88262(5) Å, c = 5.0769(11)
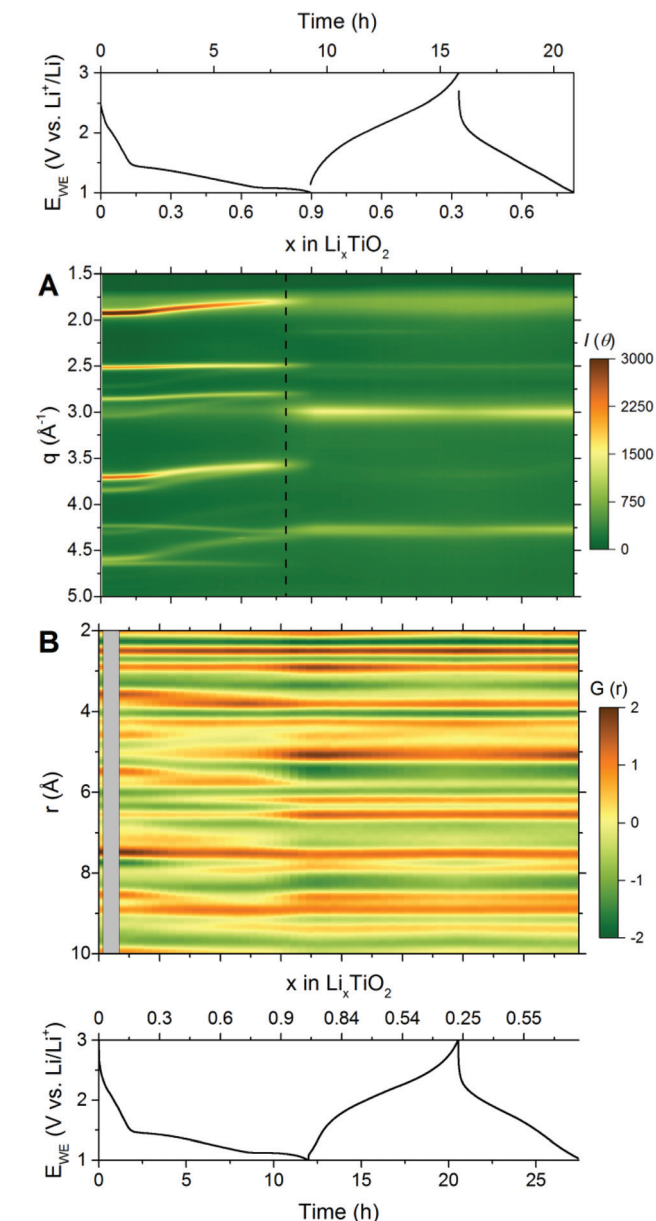

Fig. 2 Overview plots of (A) *operando* powder X-ray diffraction (λ = 0.2113 Å) and (B) *operando* pair distribution functions collected during galvanostatic battery discharge and charge of a nano-rutile TiO_2 *vs.* Li (the grey area in (B) corresponds to zero intensity due to intermittent loss of the synchrotron beam). The concurrently collected potential profiles are shown above and below the overview plots, respectively.

Å, and β = 72.575(14)° or a = 3.39(3) Å, b = 2.4345(17) Å, c = 2.938(7) Å and $\beta \sim 142.3(4)$°. However, evaluating the comparative quality of the models is very difficult (see Fig. S4, ESI†). Hence, we turn our attention to the PDF data.

From the overview plot of the *operando* PDF (Fig. 2B), it is evident that an insertion of >0.8Li per TiO_2 causes significant changes in the interatomic correlations, *i.e.* peaks are disappearing, and new peaks are emerging. This is evidence of a structural rearrangement. Hence, the monoclinic distorted $P2/m_{RUT}$ rutile-like structure transforms into a new phase with a

quite different lattice construction. To characterize the structural details of this phase, a series of three Li_xTiO_2 samples with $x \sim 0.5$, 0.8 and >1.0 were prepared by chemical lithiation of the rutile TiO_2 nanoparticles using *N*-butyl-lithium. *Ex situ* PXRD and PDFs obtained from these samples confirm that at similar degrees of Li-insertion, the same phases are obtained by chemical lithiation as by electrochemical Li-insertion in the *operando* measurement. PXRD of the chemically lithiated samples (Fig. 3A) confirms that at $xLi \sim 0.5$, $Li_{0.5}TiO_2$ remains in the monoclinic distorted ($P2/m_{RUT}$) rutile structure, while at $xLi \sim 1.0$, the sample has completely transformed into the disordered phase showing weaker and broad Bragg reflections corresponding to a crystallite size of 5.0(5) nm based on a Scherrer analysis. At $xLi \sim 0.8$, both phases are present, which confirms the two-phase transition. Raman spectra (Fig. S5, ESI†) of the chemically lithiated samples also confirm the drastic loss of crystallinity at higher lithium content, *i.e.* all Raman shifts lose significant intensity, which is an indicator of structural disordering. Performing the structural analysis using *ex situ* rather than *operando* PDF data, holds great advantage, that the samples do not contain conductive carbon and binder, which are necessary additives in the functioning electrodes for the *operando* experiments and unfortunately add to the observed PDF correlations in the lower *r*-region ($r < 5$ Å).[44]

In the PDF data (Fig. 3B), well-defined correlations are observed up to ~50 Å. The medium to long range structure (10 to 40 Å) can be modelled satisfactorily (Fig. 3B, top) by a layered monoclinic $LiTiO_2$ structure with the space group symmetry $P2/m_{HEX}$ (Table 1 and Fig. 1C), as previously suggested from X-ray and neutron diffraction as well as from theoretical predictions.[25,26] The spherical domain (or crystallite) size is estimated from the PDF fit to be 51(±17) Å, *i.e.* ~5 nm. The discrepancy that remains in the PDF fit at higher *r* (>10 Å) may arise from the anisotropic crystallite size. The characterization

Table 1 Structural parameters from a fit of the *ex situ* PDF (Fig. 3B, bottom) for the chemical lithiated nano-rutile with composition $LiTiO_2$ (corresponding to the fully discharged state) obtained using two phases: the distorted α-NaFeO₂-like structure ($P2/m_{HEX}$) and a local columbite-like structure (fitted parameters are in bold)

Main structure: α-NaFeO₂ ($P2/m_{(HEX)}$)			
Scale[a]	**0.263 (±0.065)**	ADPs[b]	
Domain diameter (Å)	**51 (±17)**	Ti U_{iso} (Å²)	**0.058 (±0.033)**
Quadr. corr. factor	**0.0 (±2.8)**	O U_{iso} (Å²)	**0.021 (±0.025)**
a (Å)	**5.12 (±0.17)**	α (deg.)	90
b (Å)	**2.902 (±0.081)**	β (deg.)	**69.0 (±1.6)**
c (Å)	**5.10 (±0.12)**	γ (deg.)	90
Atom positions			
	x	y	z
Ti	0	$\frac{1}{2}$	$\frac{1}{2}$
Ti	$\frac{1}{2}$	0	$\frac{1}{2}$
O	**0.26 (±0.10)**	0	**0.237 (±0.061)**
O	**0.23 (±0.10)**	$\frac{1}{2}$	**0.765 (±0.061)**
Li	0	0	0
Li	$\frac{1}{2}$	$\frac{1}{2}$	0

Local structure: TiO₂-II columbite			
Scale[a]	**0.737 (±0.065)**	APDs	
Domain diameter (Å)	**8.9 (±1.9)**	Ti U_{iso} (Å²)	**0.015 (±0.012)**
Quadr. corr. factor	**0.0 (±2.8)**	O U_{iso} (Å²)	**0.0041 (±0.0062)**
a (Å)	**4.63 (±0.12)**	α (deg.)	90
b (Å)	**4.76 (±0.13)**	β (deg.)	90
c (Å)	**5.42 (±0.11)**	γ (deg.)	90
Atom positions			
	x	y	z
Ti	0	0.1704	$\frac{1}{4}$
O	0.2716	0.3814	0.4142

[a] A global scale factor for the data was fitted to 0.6 (±0.2). The scale of the columbite phase was set to 1 – (scale of α-NaFeO₂). [b] ADP: Atomic Displacement Parameter.

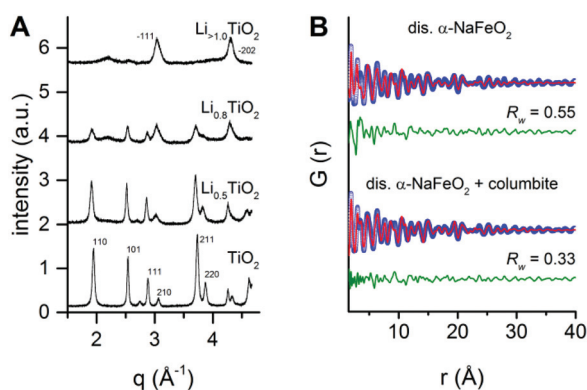**Fig. 3** (A) *Ex situ* PXRD data of pristine TiO_2 nano-rutile and chemical lithiated nano-rutile with compositions $Li_{0.5}TiO_2$, $Li_{0.8}TiO_2$ and $LiTiO_2$. Peak indexes are added for the rutile (bottom) and α-NaFeO₂ structures (top), respectively. (B) Fit of the PDF for the chemical lithiated nano-rutile with composition $LiTiO_2$. The PDFs are fitted using (top) distorted $LiTiO_2$ α-NaFeO₂-like structure ($P2/m_{HEX}$) and (below) a combination of the distorted $LiTiO_2$ α-NaFeO₂-like structure ($P2/m_{HEX}$) and a local $LiTiO_2$ columbite-like structure with a spherical diameter of 9 Å.

of the pristine TiO_2 revealed elongated particles; hence, it is likely that crystallites of the lithiated phase are also non-spherical.

The structure of the monoclinic $P2/m_{HEX}$ $LiTiO_2$ is a distorted version of the hexagonal α-NaFeO₂ prototype structure (space group $R\bar{3}m$), which is of the rock salt structure family. Thus, the layered $LiTiO_2$ structure consists of ccp layers of oxygen with titanium in half the octahedral holes and Li in the other half. The cations are ordered such that every second layer contains Ti and the others Li. The positions of Li in both rutile and layered rock salt structures have been the subject of several studies of which the majority favors octahedral coordination for Li.[17,18,21,25] On comparing the structures of $P2/m_{RUT}$ rutile-like Li_xTiO_2 and the layered $LiTiO_2$ (Fig. 1B and C), it is evident that these are linked through a translation along the *c*-axis of the Ti-atoms in every second [TiO₆] layer, *i.e.* these Ti-atoms will move to the layer above and thereby form a denser layer with the [TiO₆] octahedra connected *via* six edges as opposed to *via* two edges and six corners in rutile. This may suggest a topotactic transformation. In parallel to the translation of Ti, the oxygen arrangement is changed from hexagonal close packed in rutile to cubic close packed in the layered α-NaFeO₂-like structure. This change may be a clue as to why increasing Li-content induces the transformation from a

rutile- into an α-NaFeO$_2$-like structure. In rutile, Ti fills half the octahedral holes, and studies suggest that Li will occupy the remaining octahedral positions.[17,18,21,25] Thus, as the Li-content in the Li$_x$TiO$_2$ phase increases, the structure will approach a NiAs structure (hcp of As with all octahedral holes filled by Ni). To the extent of our knowledge, only a very few stoichiometric metal oxides adopt the NiAs structure under ambient conditions, *e.g.* Li$_2$ReO$_3$.[45] Thus, as the rutile structure approaches that of NiAs, the continued Li-intercalation forces the structure to change to a rocksalt-like structure type – in this case, the layered α-NaFeO$_2$-like structure. This analysis also implies that the composition Li$_x$TiO$_2$ is not likely to go beyond $x = 1$Li without a second major structural reconstruction as this would require Li to be intercalated into both the octahedral and tetrahedral holes in the layered Li$_x$TiO$_2$ structure.

Although the layered α-NaFeO$_2$-like ($P2/m_{HEX}$) Li$_x$TiO$_2$ structure explains the PDF correlations at higher r (>10 Å), it is evident from the difference plot (Fig. 3B, top) that some local structures ($r < 10$ Å) of a highly disordered component is not explained by the layered structure. This is especially pronounced at ~2.0 and 3.5 Å, where the layered structure lacks significant intensity. To investigate the nature of the disordered structure, a long list of TiO$_2$ and Li$_x$TiO$_2$ structures were explored as a second low-order phase. It was easily concluded that tetrahedral [TiO$_4$] coordination does not form, *i.e.* no peaks are observed in the PDF between 1.7 and 1.8 Å, where tetrahedral Ti–O distance would be found. In general, Ti is almost exclusively found in the octahedral arrangement with oxygen, and rarely in fourfold coordination with a few exceptions (*e.g.* Ba$_2$TiO$_4$).[46] Even in amorphous TiO$_2$, there are no records of tetrahedral coordination.[47] This suggests that Ti remains in six-fold coordination. The known TiO$_2$ polymorphs with [TiO$_6$]-octahedral coordination represent a wide range of ratios between corners and edges shared per [TiO$_6$] octahedra (Table 2). Edge sharing octahedra will result in a Ti–Ti nearest

neighbour distance of 2.94–3.04 Å, while the corner-sharing octahedra give rise to a broader range of distances of 3.53–3.78 Å. The number of correlations in the first and second Ti–Ti coordination shells will naturally depend on the ratios between corners and edges shared per [TiO$_6$] octahedra. In this context, the layered α-NaFeO$_2$-like structure ($P2/m_{HEX}$) and columbite TiO$_2$ polymorphs constitute the two extremes with ratios of shared corners to shared edges being 0 and 3.5, respectively. Addition of a columbite-like domain to the fit of the PDF (Fig. 3B, bottom) provides a better fit than any other TiO$_2$ polymorph (Fig. S6, ESI†). The columbite structure is built from 1D zig-zag chains of somewhat distorted edge sharing [TiO$_6$] octahedra. The chains are connected *via* corner sharing through seven corners of each octahedron. From the PDF fit, the spherical domain size of the local columbite structure is estimated to be 8.9(±1.9) Å, which corresponds to approximately two columbite unit cells along all directions. Thus, the columbite-like domains within the sample should not be regarded as a crystalline columbite structure but should be considered as small (~1 nm) domains with a structure resembling the columbite motif with the [TiO$_6$] octahedra sharing in average seven corners and two edges with neighbouring octahedra.

We would like to mention that to validate the interpretation of the PDF analysis other structural scenarios were also explored. Firstly, it was considered whether a conversion reaction takes place, *i.e.* whether a reaction between Li and TiO$_2$ occurs with the formation of Li$_2$O and Ti. The PDF shows no sign of correlations in the low r-region typical of Ti and Li$_2$O,[48,49] and this hypothesis was discarded. Secondly, the option of local disorder due to stacking faults in the layered α-NaFeO$_2$-like Li$_x$TiO$_2$ phase was investigated. In the ordered Li$_x$TiO$_2$ structure, the cations sit in the octahedral holes in-between the cp oxygen layers, which follow the ccp stacking sequence ABCABC. The cation ordering in alternating layers provides three types of octahedral environments for the cations (between layers A–B, B–C and A–C); hence, the structure is denoted as O3-type. Stacking faults would result in a combination of a ccp and hcp lattice, *e.g.* ABCBABCB. Herein, the cations can be found in two different octahedral sites (between A–B and C–B); hence, this structure is denoted as O2-type (see also Fig. S7, ESI†). An O1-type would have an ABAB O-lattice stacking sequence. This corresponds to a perfect hcp oxygen lattice, which for the composition LiTiO$_2$, where all octahedral holes are filled, represents a NiAs structure. As mentioned, no oxide with this structural type exists to the extent of our knowledge. Thus, the O1-type is omitted in the investigation of stacking faults. To model the degree of stacking faults, a combination of the O3-type and O2-type phase was fitted to the PDF in the range $r = 1.0$–14.5 Å. However, the addition of the O2-phase did not improve the fit (Fig. S8 and Table S3†), which indicates that no significant amounts of stacking faults are present.

Hence, based on the *ex situ* PDF analysis, we conclude that rutile Li$_x$TiO$_2$ transforms into a composite of ~5 nm domains of α-NaFeO$_2$-like ($P2/m_{HEX}$) Li$_x$TiO$_2$ and ~1 nm highly dis-

Table 2 Overview of a number of edges and corners shared between Ti–O6 octahedra in selected TiO$_2$ and Li$_x$TiO$_2$ polymorphs and their goodness of fit, R_w, when including the polymorph as a local structure with 10 Å spherical diameter as the second phase in the fit of the *ex situ* PDF of LiTiO$_2$ with the distorted α-NaFeO$_2$-like ($P2/m_{HEX}$) LiTiO$_2$ structure as the main phase (see Fig. 3B and Fig. S6, ESI)

Structure[a]	Edges shared	Corners shared	# shared corners : # shared edges	R_w
Columbite	2	7	3.5	0.34
Rutile	2	6	3	0.43
Brookite	3	6	2	0.38
Anatase	4	4	1	0.50
Ramsdelite	4	3	0.75	0.39
Hollandite	4	3	0.75	0.47
TiO$_2$ (B)	5	1	0.2	0.47
α-NaFeO$_2$-like	6	0	0	0.56[b]

[a] The Baddeleyite structure was also tested. Herein, Ti is coordinated by O in the trigonal prismatic geometry. This provided an agreement factor of $R_w = 0.44$. [b] The α-NaFeO$_2$-like LiTiO$_2$ is fitted as the global phase ($r = 1$–14.5 Å). The R_w value is for the fit using only this phase.

ordered columbite-like Li_xTiO_2 domains. This conclusion is cooperated by TEM analysis (Fig. 4). Here, we see that the as-prepared rutile TiO_2 and $Li_{0.5}TiO_2$ prepared by chemical lithiation contains particles of ~10 × 10 × 30 nm, which consist of one crystallite, i.e. one coherent atomic lattice extending over the entirety of most particles (Fig. 4A). After an insertion of ~1Li per TiO_2, TEM reveals that in $LiTiO_2$, the particles contain several smaller crystalline domains of different orientations separated by disordered grain boundaries of 1–2 nm (Fig. 4B). The observed TEM intensity within the domains can be matched with the α-$NaFeO_2$-like ($P2/m_{HEX}$) structure. Hence, based on TEM, the columbite-like motifs appear to constitute the grain boundaries between the layered $LiTiO_2$ domains. We note that the columbite structure has previously been reported to form as a solid–solid interphase at rutile–anatase grain boundaries.[50] Furthermore, TiO_2 columbite has been shown to be electrochemically active with a capacity of ~70 mA h g^{-1}, allowing the reversible storage of 0.2 Li per TiO_2.[51] Thus, it is likely that the columbite grain boundary takes up Li and contributes to the reversible capacity of the electrode. To further corroborate the proposed model, we hypothesized whether the Li_xTiO_2 electrode particles could instead have fractured during

discharge. This scenario would imply that the columbite-like structure forms as a surface layer on the $LiTiO_2$ α-$NaFeO_2$-like ($P2/m_{HEX}$) particles. We test this hypothesis using fracture mechanics.[40] Our analysis estimates the critical particle size below which fracture is suppressed in rutile electrodes to be $d \sim 20$ nm (see Fig. S9, ESI†). In our experiments, the electrode particles have an estimated size of $d \sim 11$ nm, which is below this critical particle size. Consequently, we reject the fracture hypothesis in our experiments.

With the knowledge obtained through the ex situ PDF and TEM analysis of the chemical lithiated samples, we can now return to the operando PDF data. Fitting the operando PDF of the fully discharged state with the α-$NaFeO_2$-like ($P2/m_{HEX}$) – the columbite model obtained from the analysis of the chemically lithiated sample provides a good fit despite the higher noise level in the operando data (see Fig. S10, ESI†). This again confirms the agreement between the structure obtained by chemical and dynamic electrochemical lithiation in this case. Thus, by sequentially fitting a series of operando PDFs using this model, we can understand the dynamic evolution during discharge–charge cycling (Fig. 5). During the initial steep potential slope up to ~0.15Li, only minor changes occur in the
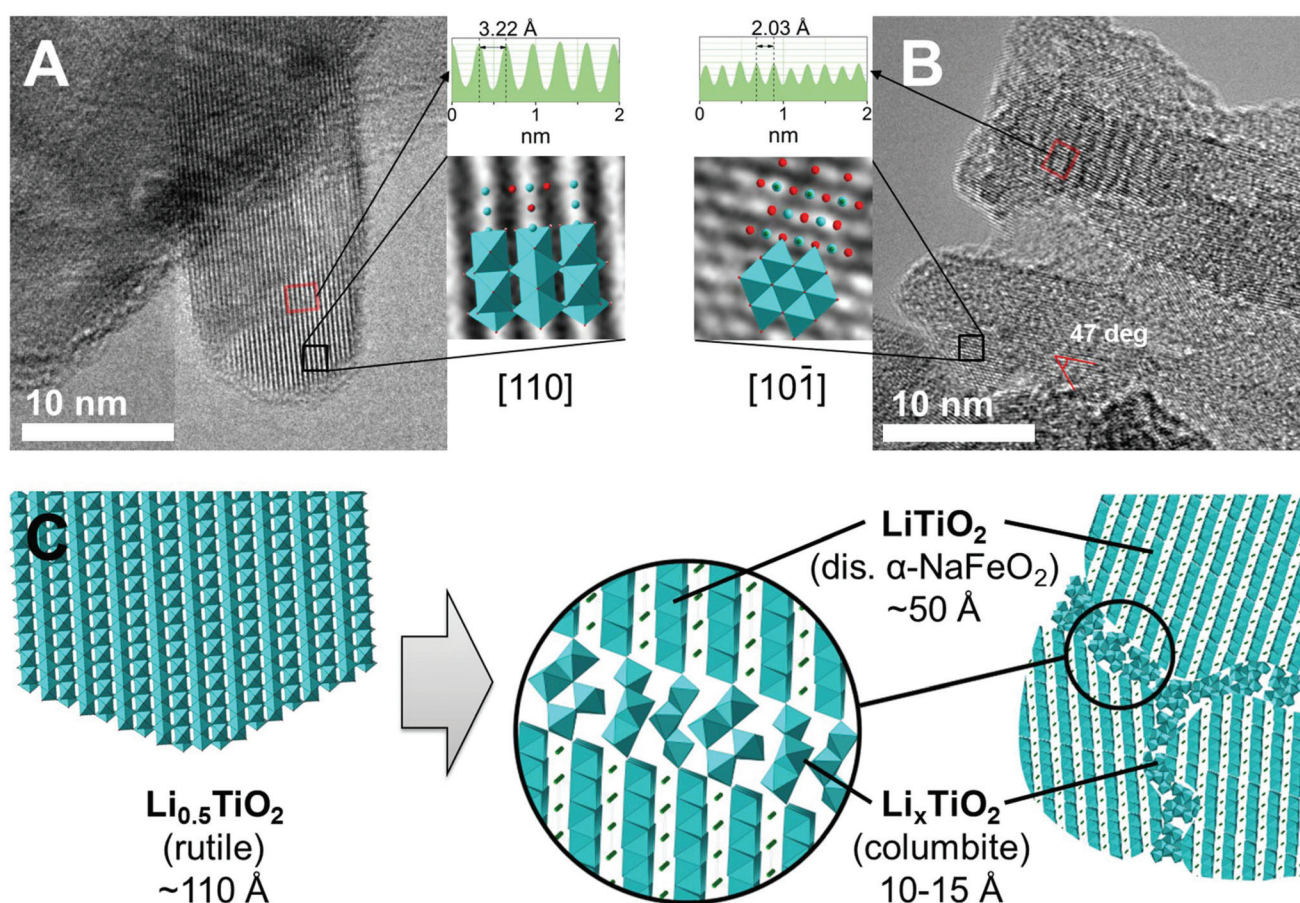

Fig. 4 TEM micrographs of nano-rutile chemically lithiated to (A) $Li_{0.5}TiO_2$ and (B) $LiTiO_2$, (C) schematic illustration of the structure and local disorder in Li-rich nano-TiO_2, showing domains of distorted α-$NaFeO_2$-like structure of ~50 Å size and local disordered regimes best described by a columbite structure of 10–15 Å and preserved the overall particle size of ~110 Å.
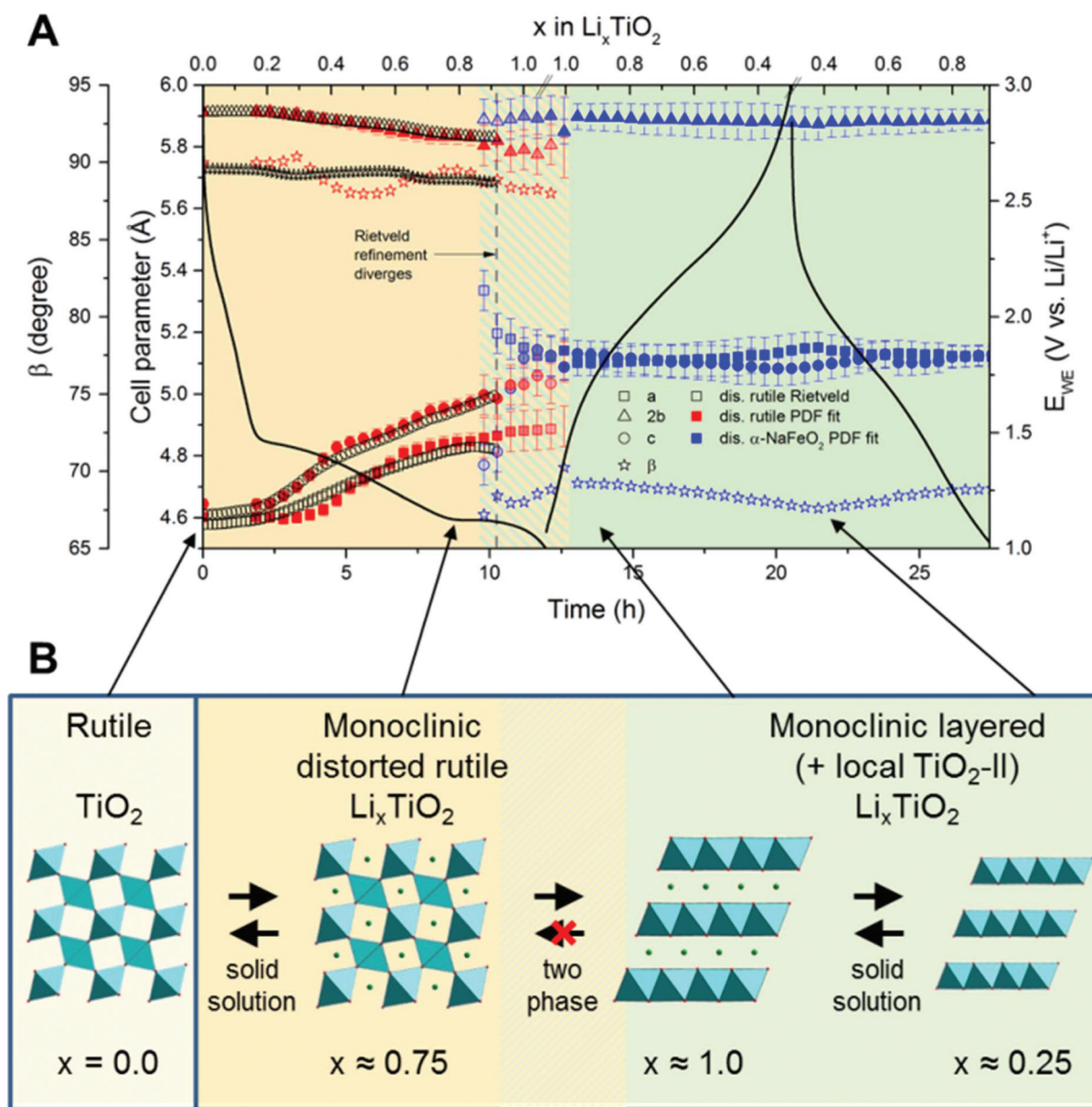
Fig. 5 (A) Evolution of the unit cell parameters (*a*, *b*, *c* and β. Note: *b*-axis plotted as 2*b* for convenience) of the monoclinic distorted rutile Li_xTiO_2 (P2/m_{RUT}, empty and red symbols) and layered α-$NaFeO_2$-like Li_xTiO_2 (P2/m_{HEX}, blue symbols) structures as a function of Li-insertion and -extraction. The values are extracted by the Rietveld refinement of the *operando* PXRD data and by fitting the *operando* PDFs. Note that at the grey dashed line, the Rietveld refinement is no longer viable due to the loss of diffraction signal. In contrast, PDF analysis allows for extracting information about the entire discharge and charge process. The electrochemical data obtained during the TXS experiment is used as a representative galvanostatic potential curve (black line). (B) Graphical illustration of the structural transformation at selected points during battery operation (size changes are not to scale).

rutile structure. Thus, the current drawn in this regime may not be related to Li-intercalation but originates from the formation of *e.g.* a solid–electrolyte interface. Between ~0.15 and ~0.8Li, rutile takes up Li *via* a solid solution reaction, which results in an increasing monoclinic distortion of the unit cell *i.e.* the *a*- and *b*-axis become increasingly different. Note that the unit cell parameters obtained by PXRD (Rietveld refinement) and PDF analysis are very similar up to the point *x*Li ~

0.78, where the Rietveld refinement fails due to too much disorder. Upon Li-insertion beyond ~0.8Li, the two-phase transition to the layered α-$NaFeO_2$-like Li_xTiO_2 domains with columbite grain boundaries initiates. The lattice misfit between the monoclinic lattice of the distorted rutile (P2/m_{RUT}) and the layered phase (P2/m_{HEX}) is very small in this transition, *i.e.* the misfit between the volume per formula unit is only ~1% and the linear misfits only ~5, ~1 and ~2%, along

the a-, b- and c-axis, respectively. The layers in the α-NaFeO$_2$-like ($P2/m_{HEX}$) phase are parallel to the ab-plane; hence, the small linear misfit along the c-axis means that the distorted rutile possibly can transform in a topotactic manner into the layered structure by a translation along the c-axis of half the Ti-atoms. The two-phase transition continues until the Li-content reaches ~1Li per TiO$_2$ in the electrode. At this composition, the lower voltage limit is reached. During recharge, ~0.8Li is extracted while the potential increases continuously without any distinct plateaus. This plateau-less behavior is also confirmed by a galvanostatic intermittent titration (see Fig. S3, ESI†). The volume of the layered Li$_x$TiO$_2$ decreases continuously during Li-extraction as expected from the decrease in ionic radius of Ti accompanying the oxidation. At the end of the charge, the composition of the phase is Li$_{\sim0.25}$TiO$_2$ and it is still maintaining the layered α-NaFeO$_2$-like structure and no sign of other phases are observed. Hence, the Li-extraction occurs *via* a complete solid solution, and it is apparent that the layered material exhibits a wide Li-stability window. At the end of the charge process, the volume per formula unit of the layered Li$_{0.25}$TiO$_2$ phase is 35.6 Å^3 per Z, which corresponds to a volume change of only 1% compared to the fully discharged state. This is significantly smaller than the volume change observed during the first discharge and in general a remarkably small volume change for an intercalation-type electrode. Typically, volume changes in intercalation electrodes are 5–10 vol%.[52,53] A small volume change is a tremendous advantage both from a mechanical point of view and in relation to limiting the formation of solid–electrolyte interface (SEI) layers, which is known to shorten battery cycle life. The latter is especially important for the anode. The second discharge follows the same solid solution pathway as observed for the charge and the process appears reversible. Galvanostatic cycling at the C/10 rate (Fig. 6) shows an initial discharge capacity of 370 mA h g^{-1}, which drops to ~220 mA h g^{-1} in the second cycle as expected from the *operando* experiments. Upon repeated cycling, a reversible discharge capacity of >200 mA h g^{-1} is maintained for 50 cycles.[54]
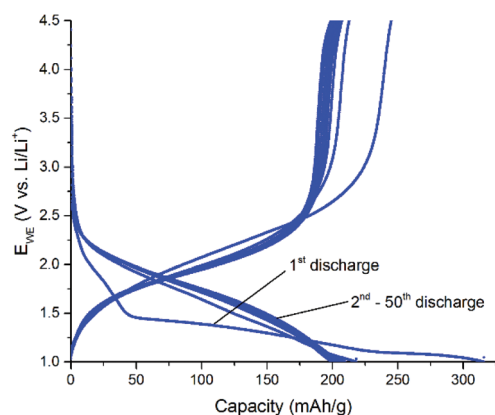

Fig. 6 Galvanostatic potential curves for 50 discharge–charge cycles of a 13 nm TiO$_2$ rutile anode *vs.* Li at the C/10 current rate.

Conclusions

The structural evolution during discharge and charge of a nano-rutile TiO$_2$ anode prepared by hydrothermal synthesis was investigated using a combination of PXRD, TXS with PDF analysis and TEM. The first discharge leads to a monoclinic distortion of the Li$_x$TiO$_2$ rutile structure, which increases with increasing Li-content. An intercalation of >0.8Li per TiO$_2$ results in an order–disorder two-phase transition with the formation of ~5 nm domains of a layered LiTiO$_2$ α-NaFeO$_2$-like ($P2/m_{HEX}$) phase with disordered grain boundaries, which can be described as ~1 nm domains of columbite-like Li$_x$TiO$_2$. The transformation from the rutile Li$_x$TiO$_2$ into the layered LiTiO$_2$ structure may be topotactic and involves a translation of the cations into separate layers and a transition from a hcp to a ccp oxygen lattice. The transition is likely driven by the fact that in a hcp oxygen lattice all octahedral holes cannot be occupied, hence it transforms into a ccp lattice. Upon recharge and subsequent cycling of the battery, the layered Li$_x$TiO$_2$ phase stores Li-ion reversibly *via* a complete solid solution reaction with a remarkably small volume change of just 1 vol% misfit between the completely charged and discharged states. The high reversible capacity of ~200 mA h g^{-1} during the 50 tested cycles, the small volume change and the ease of the material synthesis all points to the promise of this disordered anode for Li-ion battery applications.

Abbreviations

ε	Mismatch strain
γ	Surface energy
ADP	Atomic displacement parameter
APS	Advanced Photon Source
E	Elastic modulus
ccp	Cubic close packed
d	Particle size
DESY	Deutches Elektronen Synkrotron
E_{WE}	Working electrode potential
G	Energy release rate
GITT	Galvanostatic intermittent titration technique
hcp	Hexagonal close packed
PDF	Pair distribution function
PVDF	Poly(vinylidene fluoride)
PXRD	Powder X-ray diffraction
Q	Scattering vector
SEI	Solid–electrolyte interface
SR	Synchrotron radiation
TEM	Transmission electron microscopy
TXS	Total X-ray scattering
Z	Electrode geometry

Conflicts of interest

There are no conflicts to declare.

Acknowledgements

Notes and references

1 F. Fresno, R. Portela, S. Suárez and J. M. Coronado, *J. Mater. Chem. A*, 2014, **2**, 2863–2884.
2 A. Fujishima, X. Zhang and D. A. Tryk, *Surf. Sci. Rep.*, 2008, **63**, 515–582.
3 A. Kay and M. Grätzel, *Sol. Energy Mater. Sol. Cells*, 1996, **44**, 99–117.
4 B. Chen, J. Hou and K. Lu, *Langmuir*, 2013, **29**, 5911–5919.
5 M. Ni, M. K. H. Leung, D. Y. C. Leung and K. Sumathy, *Renewable Sustainable Energy Rev.*, 2007, **11**, 401–425.
6 T. Fröschl, U. Hörmann, P. Kubiak, G. Kučerová, M. Pfanzelt, C. K. Weiss, R. J. Behm, N. Hüsing, U. Kaiser, K. Landfester and M. Wohlfahrt-Mehrens, *Chem. Soc. Rev.*, 2012, **41**, 5313–5360.
7 C. Jiang and J. Zhang, *J. Mater. Sci. Technol.*, 2013, **29**, 97–122.
8 Z. Chen, I. Belharouak, Y. K. Sun and K. Amine, *Adv. Funct. Mater.*, 2013, **23**, 959–969.
9 X. Su, Q. Wu, X. Zhan, J. Wu, S. Wei and Z. Guo, *J. Mater. Sci.*, 2012, **47**, 2519–2534.
10 D. Deng, M. G. Kim, J. Y. Lee and J. Cho, *Energy Environ. Sci.*, 2009, **2**, 818.
11 Z. Yang, D. Choi, S. Kerisit, K. M. Rosso, D. Wang, J. Zhang, G. Graff and J. Liu, *J. Power Sources*, 2009, **192**, 588–598.
12 S. Takai, M. Kamata, S. Fujine, K. Yoneda, K. Kanda and T. Esaka, *Solid State Ionics*, 1999, **123**, 165–172.
13 T. Ohzuku, Z. Takehara and S. Yoshizawa, *Electrochim. Acta*, 1979, **24**, 219–222.
14 L. Kavan, D. Fattakhova and P. Krtil, *J. Electrochem. Soc.*, 1999, **146**, 1375.
15 B. Zachau-Christiansen, K. West, T. Jacobsen and S. Atlung, *Solid State Ionics*, 1988, **28–30**, 1176–1182.
16 W. J. Macklin and R. J. Neat, *Solid State Ionics*, 1992, **53–56**, 694–700.
17 M. V. Koudriachova, N. M. Harrison and S. W. de Leeuw, *Phys. Rev. Lett.*, 2001, **86**, 1275–1278.
18 M. V. Koudriachova, N. M. Harrison and S. W. De Leeuw, *Solid State Ionics*, 2003, **157**, 35–38.
19 A. Stashans, S. Lunell, R. Bergström, A. Hagfeldt and S.-E. Lindquist, *Phys. Rev. B: Condens. Matter Mater. Phys.*, 1996, **53**, 159–170.
20 C. Jiang, I. Honma, T. Kudo and H. Zhou, *Electrochem. Solid-State Lett.*, 2007, **10**, A127.
21 M. Vijayakumar, S. Kerisit, C. Wang, Z. Nie, K. M. Rosso, Z. Yang, G. Graff, J. Liu and J. Hu, *J. Phys. Chem. C*, 2009, **113**, 14567–14574.
22 P. Kubiak, M. Pfanzelt, J. Geserick, U. Hörmann, N. Hüsing, U. Kaiser and M. Wohlfahrt-Mehrens, *J. Power Sources*, 2009, **194**, 1099–1104.
23 E. Baudrin, S. Cassaignon, M. Koelsch, J. P. Jolivet, L. Dupont and J. M. Tarascon, *Electrochem. Commun.*, 2007, **9**, 337–342.
24 M. Wagemaker, W. J. H. Borghols and F. M. Mulder, *J. Am. Chem. Soc.*, 2007, **129**, 4323–4327.
25 W. J. H. Borghols, M. Wagemaker, U. Lafont, E. M. Kelder and F. M. Mulder, *Chem. Mater.*, 2008, **20**, 2949–2955.
26 M. V. Koudriachova, N. M. Harrison and S. W. De Leeuw, *Solid State Ionics*, 2004, **175**, 829–834.
27 S. J. Kim, S.-Y. Noh, A. Kargar, D. Wang, G. W. Graham and X. Pan, *Chem. Commun.*, 2014, **50**, 9932–9935.
28 M. A. Reddy, M. S. Kishore, V. Pralong, V. Caignaert, U. V. Varadaraju and B. Raveau, *Electrochem. Commun.*, 2006, **8**, 1299–1303.
29 Y. S. Hu, L. Kienle, Y. G. Guo and J. Maier, *Adv. Mater.*, 2006, **18**, 1421–1426.
30 T. A. Hewston and B. L. Chamberland, *J. Phys. Chem. Solids*, 1987, **48**, 97–108.
31 D. B. Ravnsbæk, K. Xiang, W. Xing, O. J. Borkiewicz, K. M. Wiaderek, P. Gionet, K. W. Chapman, P. J. Chupas and Y.-M. Chiang, *Nano Lett.*, 2014, **14**, 1484–1491.
32 K. Xiang, W. Xing, D. B. Ravnsbæk, L. Hong, M. Tang, Z. Li, K. M. Wiaderek, O. J. Borkiewicz, K. W. Chapman, P. J. Chupas and Y. M. Chiang, *Nano Lett.*, 2017, **17**, 1696–1702.
33 D. B. Ravnsbæk, K. Xiang, W. Xing, O. J. Borkiewicz, K. M. Wiaderek, P. Gionet, K. W. Chapman, P. J. Chupas, M. Tang and Y. M. Chiang, *Nano Lett.*, 2016, **16**, 2375–2380.
34 D. R. Sørensen, J. K. Mathiesen and D. B. Ravnsbæk, *J. Power Sources*, 2018, **396**, 437–443.
35 A. Mamakhel, C. Tyrsted, E. D. Bøjesen, P. Hald and B. B. Iversen, *Cryst. Growth Des.*, 2013, **13**, 4730–4734.
36 O. J. Borkiewicz, B. Shyam, K. M. Wiaderek, C. Kurtz, P. J. Chupas and K. W. Chapman, *J. Appl. Crystallogr.*, 2012, **45**, 1261–1269.
37 A. P. Hammersley, S. O. Svensson, M. Hanfland, A. N. Fitch and D. Hausermann, *High Pressure Res.*, 1996, **14**, 235–248.

38 P. Juhás, T. Davis, C. L. Farrow and S. J. L. Billinge, *J. Appl. Crystallogr.*, 2013, **46**, 560–566.

39 C. L. Farrow, P. Juhas, J. W. Liu, D. Bryndin, E. S. Božin, J. Bloch, T. Proffen and S. J. L. Billinge, *J. Phys.: Condens. Matter*, 2007, **19**, 335219.

40 Y. Hu, X. Zhao and Z. Suo, *J. Mater. Res.*, 2010, **25**, 1007–1010.

41 B. Lawn, *Fracture of brittle solids*, Cambridge University Press, Cambridge, 1993.

42 J. R. Rice, *J. Appl. Mech.*, 1968, **35**, 379.

43 S. T. Murphy, P. Zeller, A. Chartier and L. Van Brutzel, *J. Phys. Chem. C*, 2011, **115**, 21874–21881.

44 C. K. Christensen, D. R. Sørensen, J. Hvam and D. B. Ravnsbæk, *Chem. Mater.*, 2019, **31**, 512–520.

45 R. J. Cava, A. Santoro, D. W. Murphy, S. Zahurak and R. S. Roth, *J. Solid State Chem.*, 1982, **42**, 251–262.

46 I. D. Brown and R. D. Shannon, *Acta Crystallogr., Sect. A: Cryst. Phys., Diffr., Theor. Gen. Crystallogr.*, 1973, **29**, 266–282.

47 G. Antonioli, I. Manzini, G. Gnappi and A. Montenero, *Nucl. Instrum. Methods Phys. Res., Sect. B*, 1995, **97**, 198–201.

48 T. W. D. Farley, W. Hayes, S. Hull, M. T. Hutchings and M. Vrtis, *J. Phys.: Condens. Matter*, 1991, **3**, 4761.

49 R. A. Patterson, *Phys. Rev.*, 1925, **26**, 56–59.

50 W. N. Zhao, S. C. Zhu, Y. F. Li and Z. P. Liu, *Chem. Sci.*, 2015, **6**, 3483–3494.

51 K. Mukai and I. Yamada, *J. Electrochem. Soc.*, 2017, **164**, A3590–A3594.

52 M. T. McDowell, S. Xia and T. Zhu, *Extreme. Mech. Lett.*, 2016, **9**, 480–494.

53 R. A. Huggins, *Advanced Batteries*, Springer US, Boston, MA, 2009.

54 D. Wang, D. Choi, Z. Yang, V. V. Viswanathan, Z. Nie, C. Wang, Y. Song, J. Zhang and J. Liu, *Chem. Mater.*, 2008, 3435–3442.